J. Fluid Mech. (1976), *vol.* 73, *part* 2, *pp.* 215–240
Printed in Great Britain

A numerical simulation of Kelvin–Helmholtz waves of finite amplitude

By P. C. PATNAIK

National Center for Atmospheric Research, Boulder, Colorado 80303†

F. S. SHERMAN AND G. M. CORCOS

Department of Mechanical Engineering, University of California, Berkeley, California 94720

(Received 10 February 1975 and in revised form 1 September 1975)

A number of initial- and boundary-value problems for the Boussinesq equations are solved by a finite-difference technique, in an attempt to see how a stably-stratified horizontal shear layer rolls up into horizontally periodic billows of concentrated vorticity, such as are frequently observed in the atmosphere and oceans. This paper describes the methods, results and accuracy of the numerical simulations. The results are further analysed and approximately reproduced by a simple semi-analytic model in Corcos & Sherman (1976).

1. Introduction

There is a substantial accumulation of experimental evidence, recently reviewed by Thorpe (1973) and by Maxworthy & Browand (1975), which indicates that Kelvin–Helmholtz waves are a commonly occurring dynamic feature of the small-scale motions in the oceans and atmosphere.

Woods & Wiley (1972) identify the late stages in the process of Kelvin–Helmholtz instability with the formation of 'billow turbulence', and assert that 'mixing in the interior (i.e. away from boundary layers) of all statically stable fluids is mainly due to billow turbulence'. Garrett & Munk (1972) make a milder statement; but they formulate statistical estimates of vertical and horizontal mixing rates in a model which couples an observed spectrum of internal waves for the ocean with the notion that these waves provide the shear necessary to excite the Kelvin–Helmholtz instability. It seems to us that such attempts to parametrize mixing in a way which involves well-defined stability problems as 'building blocks' are promising, and they clearly provide one motivation for the present study and for Corcos & Sherman (1976). A successful parametrization of this small-scale transport would be a valuable contribution to our ability to predict larger-scale motions with a deterministic model, a fact which lends practical motivation to this study and many others that are closely related.

At a more abstract level, the results of this investigation may be compared with a variety of analytical predictions, to allow a closer evaluation of the effectiveness of the various approximations or assumptions upon which they are

† Present address: Science Applications Inc., 1205 Prospect Street, La Jolla, California 92037.

based, or they may suggest new approximate models. One such model is developed in Corcos & Sherman (1976).

The feasibility of numerical simulation of hydrodynamic instabilities of the sort which interest us here had been established previously, notably by Amsden & Harlow (1964), Zabusky & Deem (1971) and Christiansen (1973); but none of these authors dealt with the effects of density stratification. Laboratory experiments, in particular by Thorpe (1971), Delisi & Corcos (1973), Browand & Wang (1972) and Browand & Winant (1973), have provided much valuable information on the effects of stratification, but they do not easily yield data on velocity and vorticity fields, which are so important to the refinement of theoretical models.

A nonlinear theory of hydrodynamic stability frequently focuses on one or the other of two questions: (i) What happens to a single unstable normal-mode disturbance as it grows to finite amplitude? (ii) What interactions occur between the various normal modes that coexist in an arbitrary initial disturbance? In a laboratory experiment, it is hard to keep these questions separate, although the application of forced periodic disturbances can help. A numerical simulation allows us to separate or combine them almost at will, although it may, as in the present work, place fairly severe restrictions on the class of interaction experiments which can be studied. We have, however, been able to study the especially interesting case of the interaction of normal modes whose wavelengths stand in the ratio 2:1.

The present paper, which grew out of Patnaik (1973), starts with the specification of an initial-value problem for the Boussinesq equations. To gain computational simplicity, we follow Amsden & Harlow, Zabusky & Deem, and Christiansen in requiring that the flow be two-dimensional and periodic in the horizontal co-ordinate. Thus the instability, like that in the tilting-tube experiments of Thorpe, grows in time, not in distance downstream. The differential equations, initial conditions, and parameters of the problem are presented in § 2.

The finite-difference techniques and the numerical errors associated with their use are very briefly described and discussed in §§ 3 and 4.

The results are described in § 5, and discussed, with some brief comments on prior theoretical work, in § 6.

2. The mathematical model

We are interested in flows in which density variations are small, being dynamically important only in connexion with the gravitational body force. We suppose that the density of a given fluid particle depends solely on a single diffusing property such as temperature *or* salinity, and that the rate of density change is so small as to leave the velocity field solenoidal. Thus we base our simulation on the familiar Boussinesq equations.

Considering only strictly two-dimensional flows, and selecting Cartesian co-ordinates in which x increases horizontally and y increases vertically upwards, we write

$$\frac{\partial u}{\partial t}+u\frac{\partial u}{\partial x}+v\frac{\partial u}{\partial y}+\frac{1}{\rho_0}\frac{\partial p}{\partial x}=\nu\left(\frac{\partial^2 u}{\partial x^2}+\frac{\partial^2 u}{\partial y^2}\right), \tag{2.1}$$

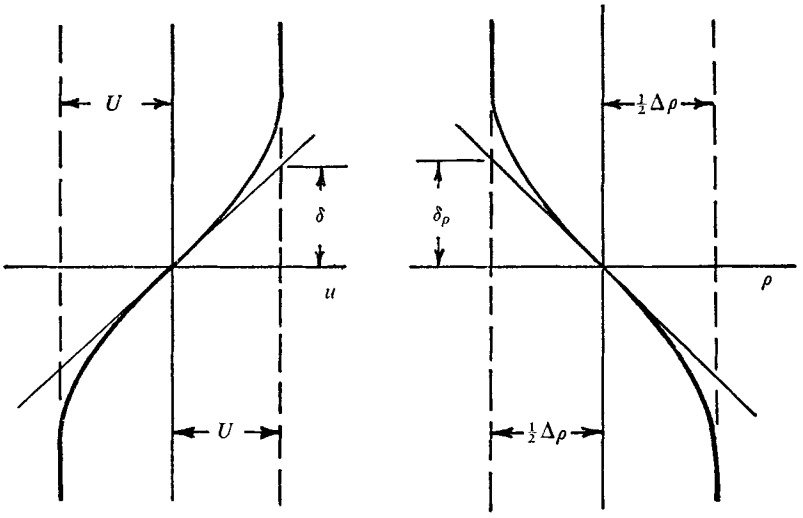

FIGURE 1. Base flow profiles at initial time.

$$\frac{\partial v}{\partial t}+u\frac{\partial v}{\partial x}+v\frac{\partial v}{\partial y}+\frac{1}{\rho_0}\frac{\partial p}{\partial y}=\nu\left(\frac{\partial^2 v}{\partial x^2}+\frac{\partial^2 v}{\partial y^2}\right)-\frac{\rho}{\rho_0}g, \tag{2.2}$$

$$\frac{\partial \rho}{\partial t}+u\frac{\partial \rho}{\partial x}+v\frac{\partial \rho}{\partial y}=\beta\left(\frac{\partial^2 \rho}{\partial x^2}+\frac{\partial^2 \rho}{\partial y^2}\right), \tag{2.3}$$

$$\frac{\partial u}{\partial x}+\frac{\partial v}{\partial y}=0. \tag{2.4}$$

The kinematic viscosity ν, the diffusion coefficient for density changes β, and the mean density for the flow field of interest ρ_0 are all taken to be constant.

We wish to study the instability of an isolated horizontal layer, across which the horizontal velocity and fluid density change from $-U$ to $+U$ and from $\rho_0+\frac{1}{2}\Delta\rho$ to $\rho_0-\frac{1}{2}\Delta\rho$ as the layer is crossed from below to above. The density difference is gravitationally stabilizing (i.e. $\Delta\rho > 0$).

The specific 'base flow' to which the initial perturbations were added was that which would be brought about by molecular diffusion from initial coplanar discontinuities of density and horizontal velocity at $y = 0$. Thus the base-flow profiles are

$$u = U\,\mathrm{erf}\,(\pi^{\frac{1}{2}}y/2\delta), \quad \rho = \rho_0 - 0{\cdot}5\Delta\rho\,\mathrm{erf}\,((\pi Pr)^{\frac{1}{2}}y/2\delta).$$

These introduce $Pr = \nu/\beta$, and define δ as half the maximum-slope thickness of the base-flow velocity profile, at time $t = 0$.

$$\delta = U/(du/dy)_{\max}.$$

(See figure 1.)

We do not think that the exact shape of these profiles has much effect on the subsequent development of the flow, but it is important that, in all cases we ran, Pr was small enough that the local Richardson number

$$J(y) = \frac{-g\,d\rho/dy}{\rho(du/dy)^2}$$

Re	*J*	α	*Re*	*J*	α
25†	0·03	0·20	50	0·15	0·43
50	0·03	0·20	100	0·15	0·43
100	0·03	0·20	200	0·15	0·43
50‡	0·07	0·20	100*	0·20	0·43
100‡	0·07	0·20	1600	0·20	0·43
100	0·15	0·30	50*	0·15	0·60
50	0·03	0·43	100*	0·15	0·60
100	0·03	0·43	200	0·15	0·60
50	0·07	0·43	50	0·07	0·65
100	0·07	0·43	100	0·07	0·65
200	0·07	0·43	200	0·07	0·65
			50§	0·07	0·43 + 0·215

TABLE 1. Parameters of the simulations. For all cases $Pr = 0{\cdot}72$. † Extended run. ‡ Run at two different initial amplitudes. * Apparently neutral or slightly stable. § Interaction runs.

reached a single minimum at $y = 0$. Thus the waves that appear here are of the type which Browand & Wang (1972) aptly called Rayleigh waves.

To the base flow we added an initial disturbance, which is an unstable eigensolution of the Taylor–Goldstein equation, adjusting the amplitude of the disturbance so that the maximum initial slope of any curve of constant density assumed a prescribed value (usually $-0{\cdot}2$, occasionally $-0{\cdot}1$). The necessary eigensolutions were generated by the numerical techniques employed by Michalke (1965). Again, we do not expect that the exact form of the initial disturbance has much effect on the finite amplitude stages of development.

For all times, we impose boundary conditions that require the disturbances to be periodic in x and to vanish as $|y| \to \infty$. In the numerical simulation, the velocity and density perturbations are required to vanish at $|y| = 0{\cdot}625\lambda$, where λ is the wavelength of the disturbance. It was found that application of these boundary conditions at larger values of $|y|$ only wasted computer time and storage, without measurably influencing the computed results.

Aside from the Prandtl or Schmidt number, ν/β, the primary effect of which is seen in the relative thicknesses of the initial shear layer and pycnocline, each simulation is characterized by the following parameters:

Reynolds number

$$Re = U\delta/\nu;$$

Minimum Richardson number

$$J = g_*\delta(Pr)^{\frac{1}{2}}/(2U^2)$$

(where $g_* \equiv g\Delta\rho/\rho_0$); and dimensionless disturbance wavenumber

$$\alpha = 2\pi\delta/\lambda.$$

This particular set of parameters is chosen because of its common appearance in the linear theory, although we shall see that λ is for some purposes a better reference length than δ for the scaling of buoyancy forces in the nonlinear

development of vigorous instabilities. We shall also use λ/U as a scale for time in the presentation of results.

Table 1 presents the combinations of parameters for which simulations were made. They explore the ranges of Re, J and α that permit initial instability, and within which variation of each parameter has a substantial effect on the large-scale features of the disturbed flow. It would have been of considerable physical interest to explore the effects of higher Reynolds number on the smaller-scale features of the instability, but we could not afford to employ the very fine computational mesh required to give a faithful rendering of these details.

3. The numerical simulation

The domain $0 \leqslant x \leqslant \lambda$, $-0{\cdot}625\lambda \leqslant y \leqslant 0{\cdot}625\lambda$ was subdivided by a rectangular mesh, with 32 equal increments of x. Most runs made with 56 increments of y, the outer 24 being equal to the x increment, while the inner 32 were half that size. Velocity components, densities and pressures are all defined at the mesh intersections. All x derivatives were represented by second-order centred differences; so were all y derivatives, except those at the top and bottom boundaries, where second-order one-sided differences were used.

The algorithms employed are basically those of Chorin (1968). In short, Chorin's method employs the primitive variables, u, v, ρ, and p, and marches forward in time in the following manner.

First u, v and ρ are advanced through a time step Δt to auxiliary values, under the influence of convection, diffusion and gravity, but ignoring the effect of pressure forces. This step is taken implicitly in time, using the Peaceman–Rachford (Alternating-Direction-Implicit) algorithms.

This completes the advancing of ρ, but the auxiliary values of u and v do not satisfy the continuity equation, and p has not yet been advanced at all. The latter two shortcomings are simultaneously overcome by an iteration process, in which the difference between successive iterates for p is set proportional to the local value of $\nabla . \mathbf{u}$ at that stage of the iteration, while each new iterate for u or v is found by adding to the corresponding auxiliary value an increment due to the local value of the pressure gradient, evaluated from the current iterate for p.

The method has been carefully analysed for stability and convergence by Chorin (1969). Further algorithmic and/or programming details may be obtained by direct correspondence with the first author.

4. Accuracy of the simulation

The accuracy of substituting the Boussinesq equation for a more complete version of the Navier–Stokes equations is well established in related problems such as free convection. What concerns us here are the numerical aberrations which are part of any finite-difference scheme for approximate solution of partial differential equations.

Patnaik (1973) described a number of detailed checks made to ensure that the numerical procedures were free of systematic flaws, and that the x, y, and t

increments were small enough that the large-scale flow patterns shown here can be believed to be accurately represented. Rather than describe these tests here, we announce the good news that Patnaik has recently been able to reproduce these results very closely with a new set of algorithms which differs in almost every respect from those employed in his original work.† In a typical run ($Re = 100$, $J = 0{\cdot}07$, $\alpha = 0{\cdot}43$) the two numerical schemes give predictions of maximum billow amplitude, and of the time to reach it, which differ by only about 1 %.

To determine whether small-scale details revealed by the simulations are physically real, or numerical artifacts, is a much harder task. Details that vanish when the mesh is refined are presumably non-physical, but one is always left wondering about those remaining when the process of refinement has run up against financial or computer-capacity limits.

A simple physical test, which was useful in our work, can be made on local values of the density. Equation (2.3), together with the boundary conditions, shows that ρ can never attain values more extreme than those appearing in the initial field. In *barotropic* two-dimensional flow we could make a similar statement about the vorticity, and even in our study, where baroclinic generation of vorticity is very important, we can sometimes spot unphysical vorticity values. For example, since Ω (the vorticity) is initially everywhere negative, any positive values which appear at later times must be unreal unless they can be clearly traced to baroclinic generation.

The principal fruit of these physical tests was to reveal that the profiles of very thin shear layers, which develop with time for many combinations of parameters, are distorted by 'diffraction fringes' of numerical origin if the true profile of the layer would have had to be resolved by less than about six or seven mesh points. Examples of this type of distortion are prominent near the left and right edges of figure 7(*c*). Suspicious wiggles of presumably similar origin can be seen in some of the vorticity maps of Zabusky & Deem.‡

Finally, it will be recognized that most of our figures have been plotted by the computer. The plotting algorithms we employed can occasionally be fooled into representing a long narrow peninsula as a chain of islands. This phenomenon, which has no basis in the numerical output from the computer, is well illustrated in figure 4(*c*).

5. Results

To describe partly the wealth of information provided by the numerical simulations, we depend heavily on maps of various flow quantities, plus curves that represent the time evolution of prominently observable local or integral quantities.

† In the new scheme, which is rather like that of Zabusky & Deem, u, v, p and ρ are defined on a staggered grid; 'Arakawa differencing' of convective derivatives is used; the first fractional time step is taken explicitly rather than implicitly; and the Poisson equation that arises as we advance the pressure is solved by Fast Fourier Transform rather than by relaxation.

‡ Look e.g. in about the middle of Zabusky & Deem (1971, figure 8(*b*)).

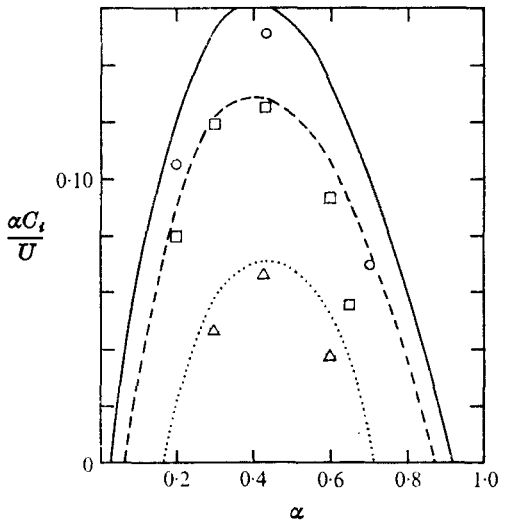

FIGURE 2. Initial growth rates. Data from this study. $Re \equiv U\delta/\nu = 100$. J: ○, 0·03; □, 0·07; △, 0·15. Linear, viscous theory by Maslowe. J: ——, 0·03; – – –, 0·07; · · ·, 0·15.

5.1. *Wave growth at early times*

While criticism of linear stability theory as applied to a time-dependent base flow was not our prime goal, we did compute a 'wave energy' from

$$E(t) = \int_{-0{\cdot}625\lambda}^{0{\cdot}625\lambda} dy \left(\int_0^{\lambda} \frac{(u-\overline{u})^2 + v^2}{2}\, dx \right), \tag{5.1}$$

and observed that it grew approximately exponentially with time when it was small. This invited the comparison with 'linear growth rates' shown in figure 2, in which the curves represent calculations kindly done for us by Maslowe, by the methods described by Maslowe & Thompson (1971). The ordinate in figure 2 was found from

$$\frac{\alpha c_i}{U} = \frac{\delta}{2U} \frac{d}{dt} (\ln E).$$

Several observations need to be made, lest this comparison be taken too seriously. In the first place, we defined the $\overline{u}$ which appears in (5.1) by

$$\overline{u}(y,t) = \frac{1}{\lambda} \int_0^{\lambda} u\, dx,$$

so that it is a property of the *mean* flow, rather than of the time-dependent *base* flow. Had our simulations been started at sufficiently small perturbation amplitudes, the mean flow and the base flow should have been indistinguishable. In fact, the mean flow 'diffused' in the y direction somewhat faster than did the base flow.

Furthermore, the x variation of the disturbance departed noticeably from a simple sine wave during the time of approximately exponential growth of E, and a growth rate determined from the variation of the maximum elevation of the isopycnic surface $\rho = \rho_0$ differed appreciably from the value found from $E(t)$.

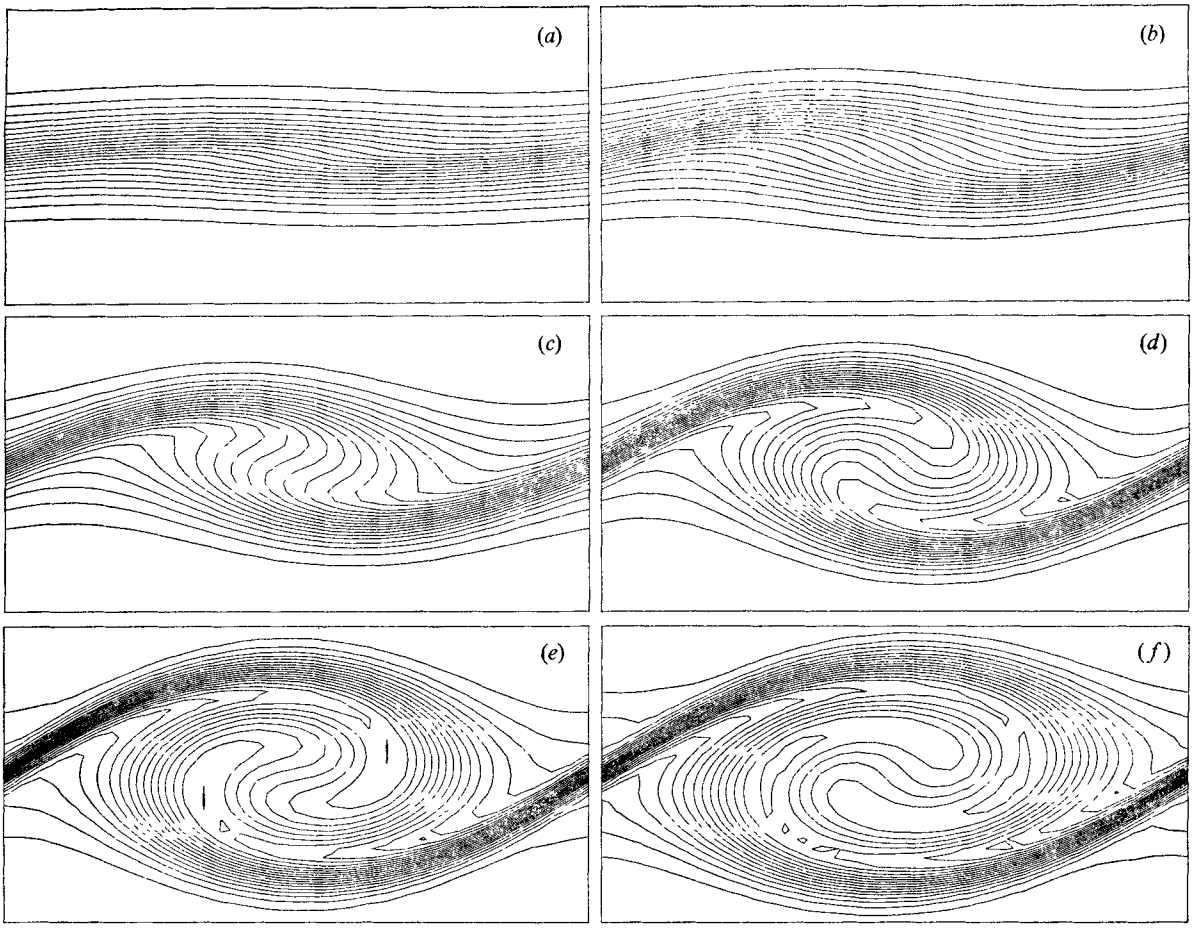

FIGURE 3. Isopycnic contours as function of time. $Re = 100$, $J = 0{\cdot}07$, $\alpha = 0{\cdot}43$, $\tau \equiv Ut/\lambda$. τ: (*a*) 0, (*b*) 0·5, (*c*) 1·0, (*d*) 1·5, (*e*) 2·0, (*f*) 2·42, time of maximum amplitude.

We note that the range of E over which $d(\ln E)/dt$ is approximately constant was very small (only about 15 %), and conclude that our simulations do *not* begin with disturbances small enough so that a critical comparison can be made with linear theory. Finally, we remember that our initial perturbation is not a normal-mode solution of the linearized Boussinesq equations, but was derived from a linear theory which neglects viscosity and diffusive changes of density. Hence our solutions at very early times presumably involve a little reshaping of the initial perturbation. Thus, the comparison shown in figure 2 is neither strictly a test of the validity of linear theory, nor of the accuracy of the nonlinear computations.

One noteworthy qualitative feature of the solutions at early times is the nearly immediate eradication of the unphysical double maximum of vorticity, which appears along the deformed locus of the surface on which $\rho = \rho_0$ when linear theory is used to describe an initial disturbance of fairly large amplitude and relative wavelength. (See e.g. Michalke 1965.) The tendency of our solutions (see e.g. the top two panels of figure 13) is to define a band within which the

vorticity is everywhere nearly equal to a single maximum which appears, if anywhere, at about $x = \frac{1}{2}\lambda$, $y = 0$. This band is thinned at $x = 0$ and λ and fattened at $x = \frac{1}{2}\lambda$, and corresponds qualitatively very well with the early-time pictures sketched by Batchelor (1967) and exhibited in numerical simulations of Christiansen (1973).†

5.2. *General evolution of the flow field during billow growth*

Figure 3 shows a sequence of isopycnic patterns for a wave which has the preferred wavelength for fastest growth according to linear theory. The Reynolds number is high enough that isopycnic surfaces do not differ greatly from material surfaces during the time elapsed, and the pictures bear good qualitative resemblance to what one sees in the laboratory with smoke or dye tracers.

The prominent qualitative features of the process are the rolling-up of isopycnic contours in the region we shall subsequently call the *cores*, and the crowding of these contours along inclined bands, which we shall call the *braids*, that connect the bottom of one core to the top of the next.

Stream function and vorticity are readily computed from mesh-point values of u and v. In figure 4, contour maps for these quantities are compared with that for density, for the 'climax' state of maximum wave amplitude.

The streamline pattern is of the cat's-eye form at all times. The surface on which $\rho = \rho_0$, which is darkened in figure 4 (*a*) and dashed in 4 (*b*) and (*c*), coincides almost exactly with the departing branch of the dividing streamline that outlines the cat's eye in 4 (*b*), and with the crest line of the ridge of high vorticity values in 4 (*c*), between the stagnation point at (0, 0) and the point, $x \simeq \frac{1}{2}\lambda$, $y = H$, at which all of these loci reach their maximum vertical displacement. This coincidence is not typical of the entire period of vigorous wave growth, during most of which the locus of the braid (whether defined by $\rho = \rho_0$ or by a sectional maximum of vorticity) lies slightly inside the cat's eye.

By close inspection of figure 4 (*c*), we can make some interesting observations. These start with one which is unfortunately not documented in the figure, but which can be deduced from the simulation of Christiansen (1973), and which we have confirmed with the model presented in Corcos & Sherman (1976). However, we support the conclusion, it appears that virtually all the fluid that comprised the unperturbed shear layer has moved into the cores by the time the climax state is reached. Thus, the 'topography' of the vorticity field, in which high ridges (the braids) are separated from a high rounded hill (the core) by relatively low 'cols' or 'passes', is largely shaped by baroclinic effects. Virtually all the vorticity remaining in the braids has been baroclinically generated. The fluid bearing this vorticity follows that of the initial shear layer into the cores, but in so doing it assumes a configuration, in the area of the 'passes', where baroclinicity produces vorticity of the opposite sign. Indeed, by noting that in the vorticity equation, which can be derived by cross-differentiation of (2.1) and (2.2), the baroclinic source term is equal to $-(g/\rho_0)\,\partial\rho/\partial x$, we can make sense of the variation of Ω all along the locus $\rho = \rho_0$, which has been dotted into figure 4 (*c*)

† See Batchelor (1976, p. 516); Christiansen (1973, figure 5, third panel).

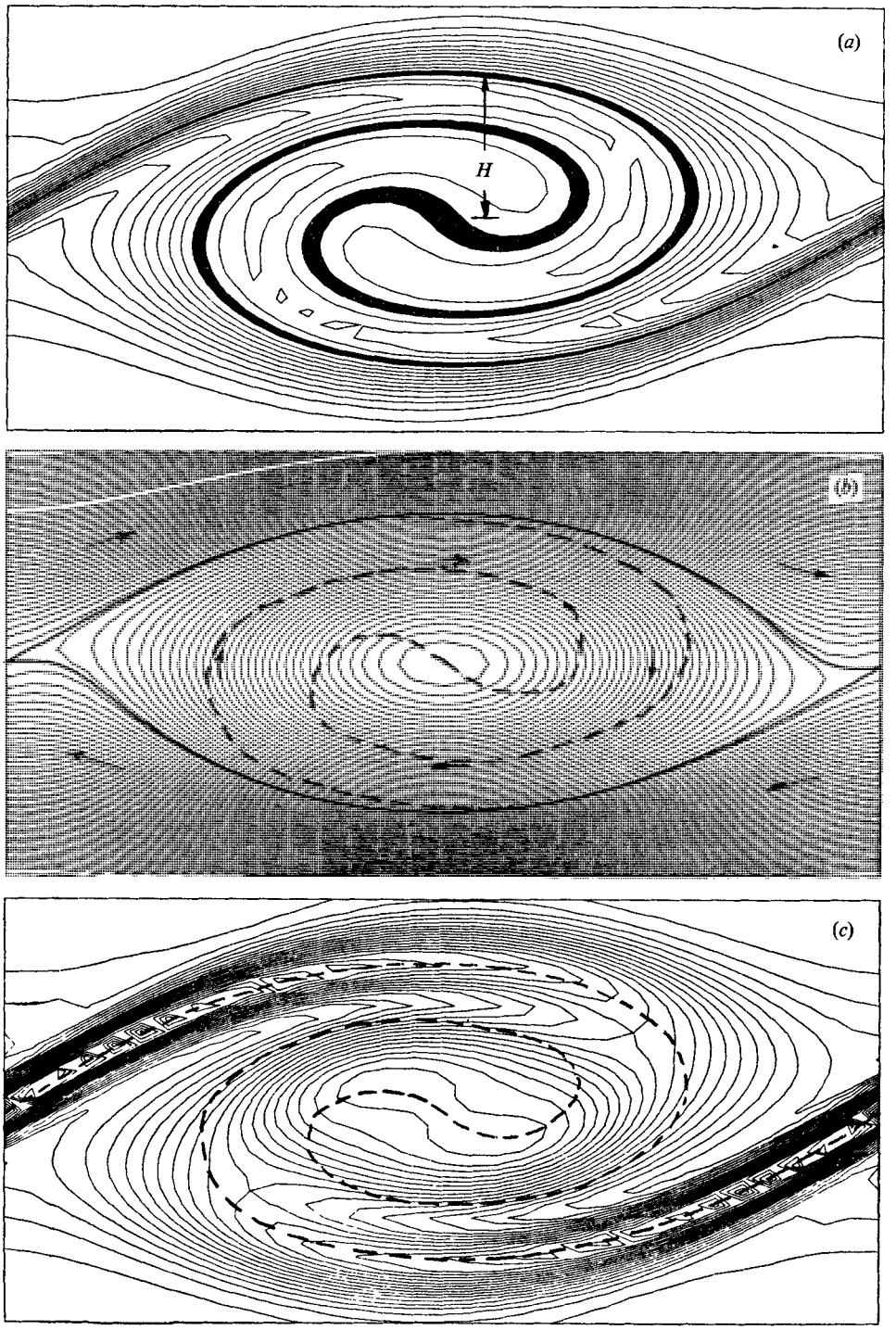

FIGURE 4. The climax states. $Re = 100$, $J = 0{\cdot}07$, $\alpha = 0{\cdot}43$. (*a*) Isopycnic contours ($\rho \simeq \rho_0$ darkened). (*b*) Streamlines (cat's eyelid darkened). (*c*) Iso-vorticity contours. (Peak value in braid $= -10{\cdot}8$, peak value in core $= -9{\cdot}5$.) The contour $\rho = \rho_0$ is dashed for reference in (*b*) and (*c*).

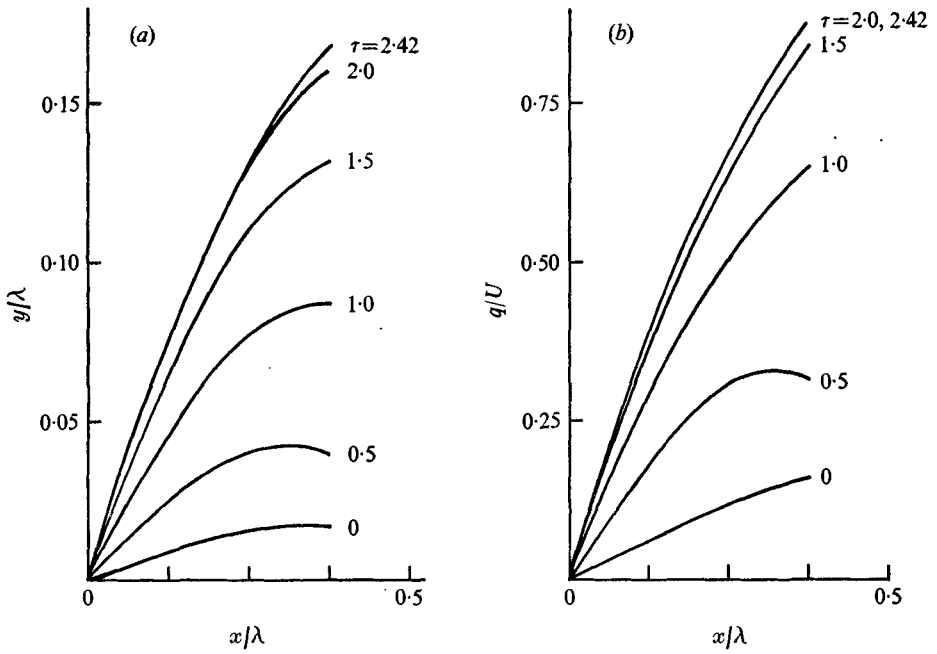

FIGURE 5. Kinematics of the braid. $Re = 100$, $J = 0{\cdot}07$, $\alpha = 0{\cdot}43$. (*a*) Locus of the braid at various times. (*b*) Velocity along the braid at various times.

for this purpose. Remember that this is a locus along which Ω would be constant if there were no diffusive mechanisms or baroclinicity.

Along the braid itself, $|\Omega|$ decreases slightly as distance from the stagnation point increases. This is consistent with a decreasing rate of baroclinic generation as the inclination of the braid decreases, although there are almost certainly other more subtle advective and diffusive effects. When the locus of $\rho = \rho_0$ dips down, so that $\partial\rho/\partial x$ changes sign, $|\Omega|$ is decreased by baroclinic action, and this continues almost exactly to the point at which the locus starts to rise again. Thereafter, $|\Omega|$ increases steadily until the locus makes a final dip in passing through the centre of the core. There is even a hint, in the hour-glass shape of the innermost equi-vorticity contour, that this final dip has had an effect.

We may have placed undue faith in the numerical accuracy of local vorticity values in making the foregoing observations, or we may have strengthened that faith because the observations seem not unreasonable. In any event, it appeared from detailed studies of typical error patterns (the 'diffraction fringes' referred to in § 4) that an integral measure of braid vorticity, which we shall call the 'braid shear',

$$S(x,t) = [\cos\theta_B(x,t)]\int_{-\infty}^{\infty}\Omega(x,y,t)\,dy$$

may be reasonably accurate, because positive and negative local errors in Ω approximately cancel. $S(0,t)$ gives an interesting characteristic of the braid, which can be predicted by the model in Corcos & Sherman (1976).

We see from the streamline patterns, figure 4(*b*), that the braid is being

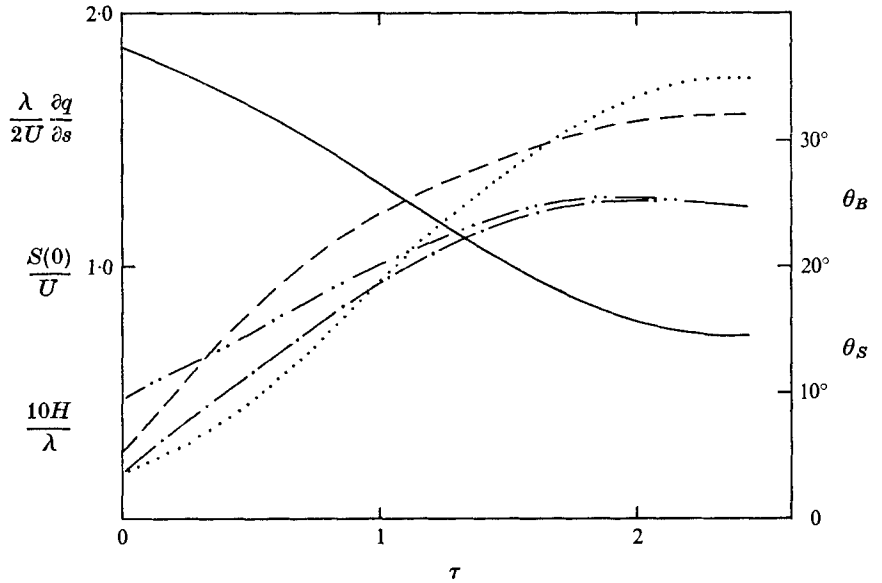

FIGURE 6. History of braid properties. $Re = 100$, $J = 0{\cdot}07$, $\alpha = 0{\cdot}43$. ——, shear across braid at $x = 0$, S/U. – – –, rate of stretching of braid at $x = 0$, $(\lambda/2U)(\partial q/\partial s)$. —·—, slope of braid at $x = 0$, θ_B. —· ·—, slope of departing streamline at $x = 0$, θ_S. · · ·, maximum elevation of braid, $10H/\lambda$.

stretched and thinned. Further observations, in particular of the straightness and slenderness of the braid, strongly suggest that this deforming motion is induced by the vorticity which is more or less concentrated in the cores, and not by the vorticity in the braid itself. (Obviously the boundary between braid and core is not sharp, and its location is fairly arbitrary. To be definite, let us take it at $x = \pm\frac{1}{2}\lambda$, $y = H$.)

Since the rate of stretching of the braid plays a key role in the model presented in Corcos & Sherman (1976), we present some data from this same case, in figure 5. The locus of the braid at various times is shown in figure 5(*a*); the corresponding distributions of velocity tangential to that locus are shown in figure 5(*b*). The rate of stretching ($\partial q/\partial s$, where s is arc length along the braid) is roughly constant over about half the length of the braid, and varies little with time during the latter half of the rolling-up process.

Finally, in figure 6, we show how various salient properties of the braid, and of the streamline with which it nearly coincides, vary with time, during the growth process shown in figure 3. The angle of the braid and of the streamline at (0, 0), the rate of stretching of the braid at that point, and the maximum vertical displacement of the braid grow in a roughly similar fashion, while the shear across the braid drops from its initial value to about 40 % of that value. The braid shear that remains at $\tau = 2{\cdot}4$ is essentially all of baroclinic origin in this case.

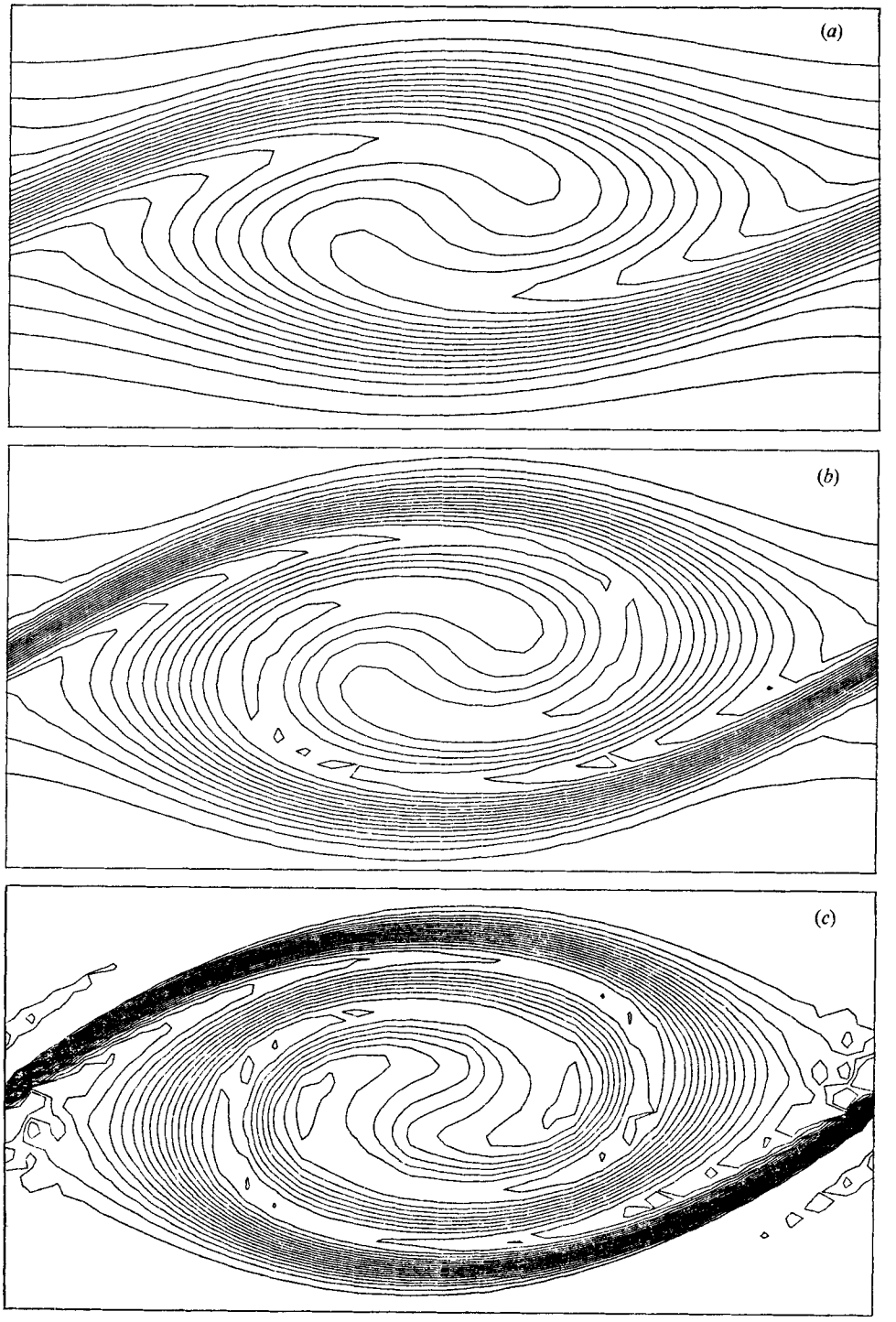

FIGURE 7. Effects of Reynolds number on the climax isopycnics.
$J = 0{\cdot}07$, $\alpha = 0{\cdot}43$. *Re*: (*a*) 50, (*b*) 100, (*c*) 200.

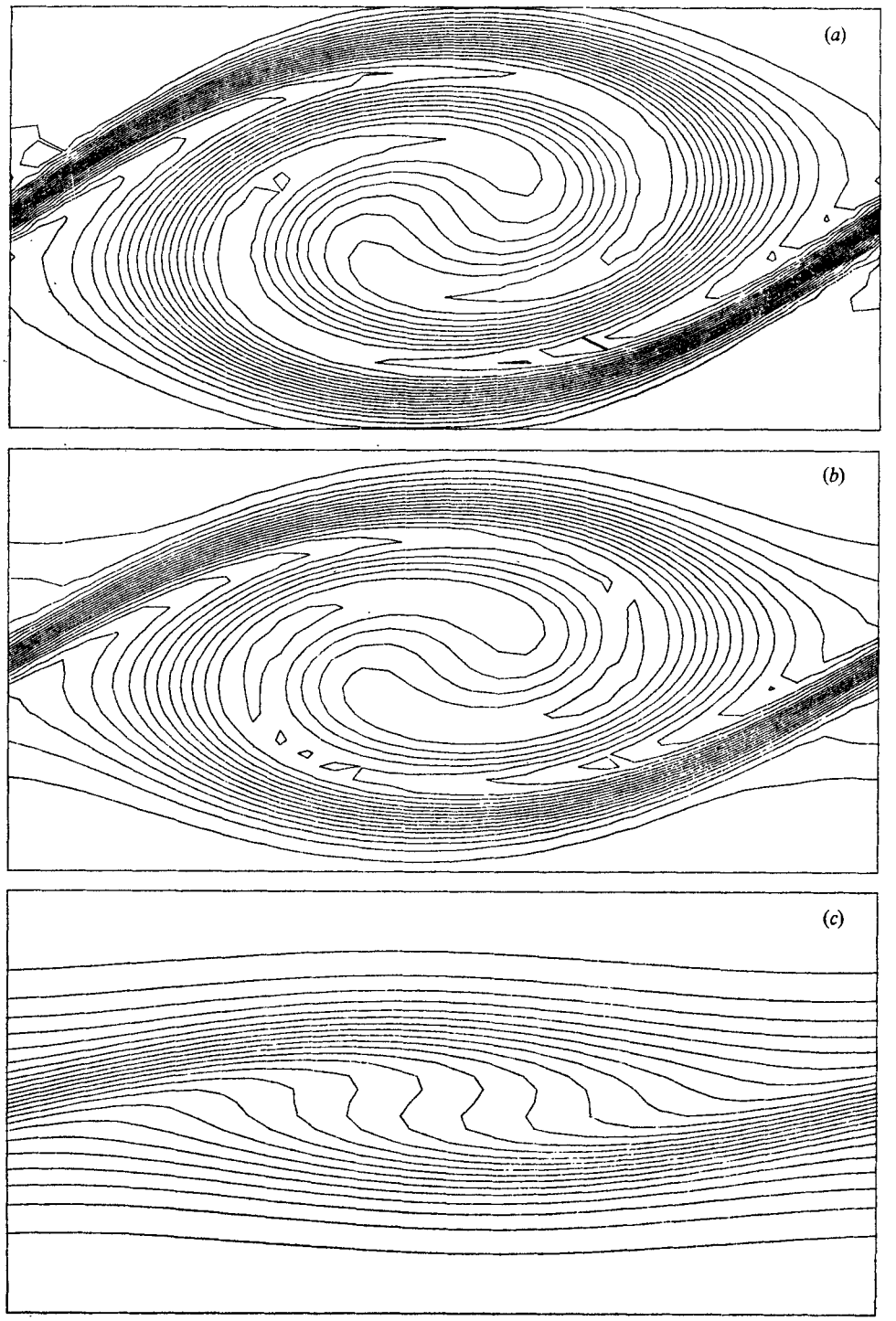

FIGURE 8. Effect of Richardson number on the climax isopycnics.
$Re = 100$, $\alpha = 0{\cdot}43$. J: (*a*) 0·03, (*b*) 0·07, (*c*) 0·15.

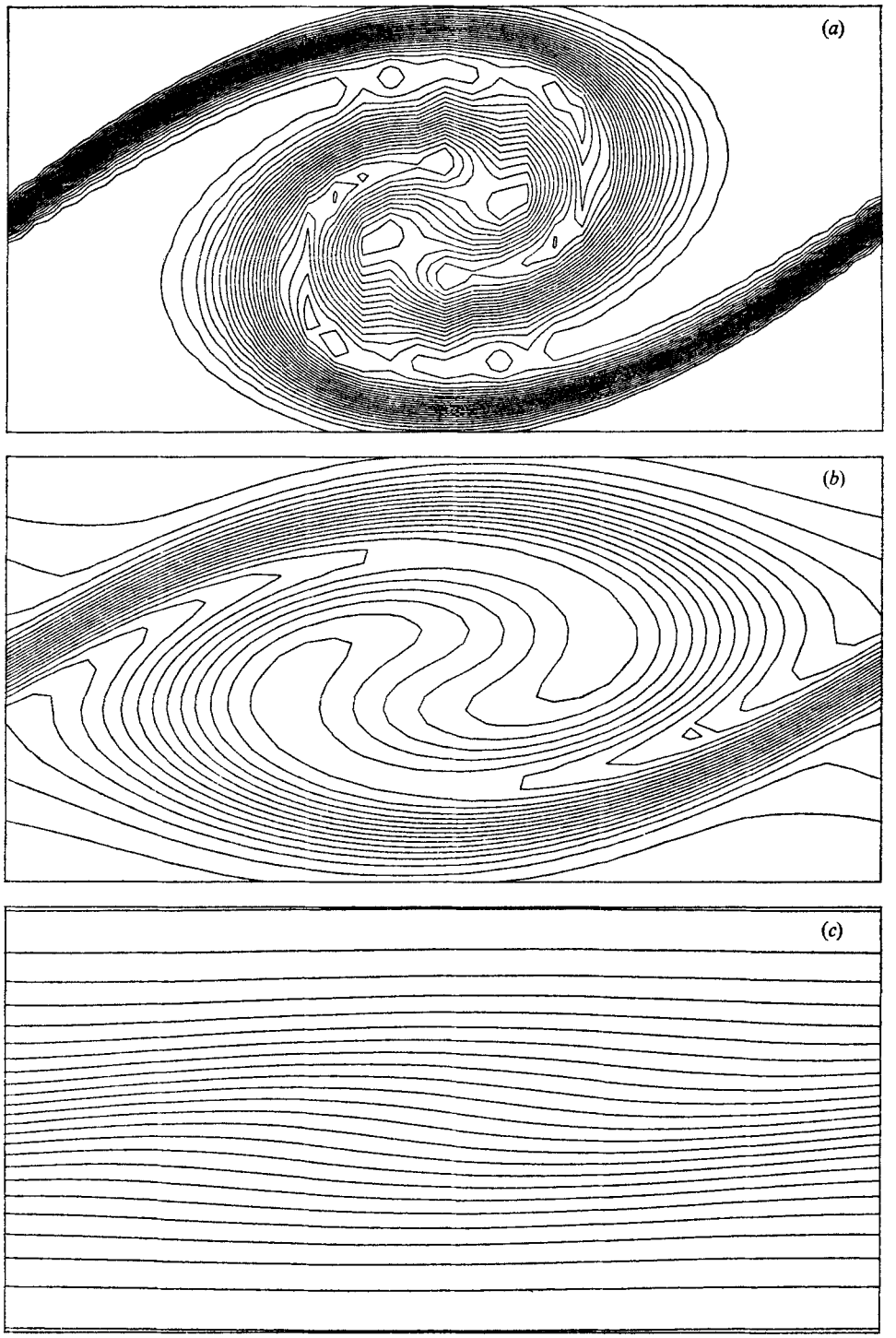

FIGURE 9. Effect of wavelength on the climax isopycnics.
$Re = 50$, $J = 0{\cdot}03$. α: (*a*) 0·2, (*b*) 0·43, (*c*) 0·7.

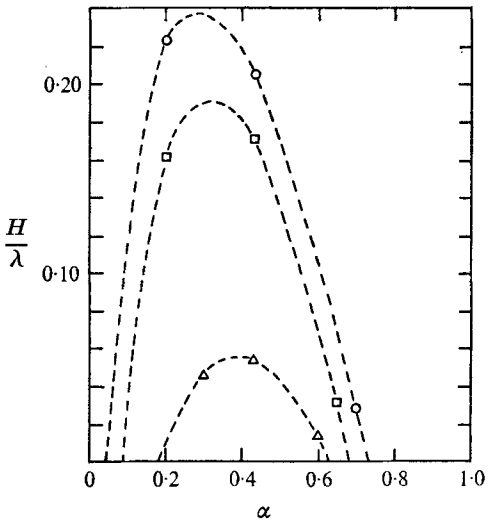

FIGURE 10. Effect of wavelength on braid displacement.
$Re = 100$. J_0: ○, 0·03; □, 0·07; △, 0·15.

5.3. *Effect of parameters on the disturbance in the climax state*

All of the flow simulations in which the initial disturbance grew markedly were qualitatively similar to that just described. Their quantitative differences are indicated by the maps of isopycnic surfaces shown in figures 7–9, and by the data plotted in figures 10–12, all of which refer to the 'climax' state.

Figure 7 indicates that diffusive mechanisms have little effect on the gross features of the instability, even for these moderately low Reynolds numbers, but that they determine, in a competition with advective effects, the thickness of the braids and the sharpness of density contrasts which persist in the core, where fluid from the original pycnocline is intertwined with entrained fluid.

Figure 8 shows how gravitational stability stunts the growth of the billow, even well before $J = 0{\cdot}25$. Figure 9 is in some ways the most startling, showing that nonlinear processes favour the development of waves longer than those that grow fastest in the linear range, while waves that grow slowly in the linear range because of their shortness stop growing at very small amplitudes, and never develop the characteristic rolled-up appearance of longer waves.

The effect of α on H/λ of the climax state is explicitly shown in figure 10, which should be compared with figure 2. At first glance, the data trends look almost identical, but closer inspection shows how nonlinear effects have favoured the growth of the longer waves. The interpolation curves have been brought to $H/\lambda = 0$ at a long-wave cut-off provided by Kelvin's linear theory for a shear layer of zero thickness. This criterion, $k = g_*/2U^2$, becomes $\alpha = J/Pr^{\frac{1}{2}}$ after multiplication of both sides by δ.

Figure 11 shows effects of Re and J on H/λ in the climax state. The principal features are the expected strong stabilizing effect of increasing Richardson number, and the relatively low values to which Re must drop before viscosity

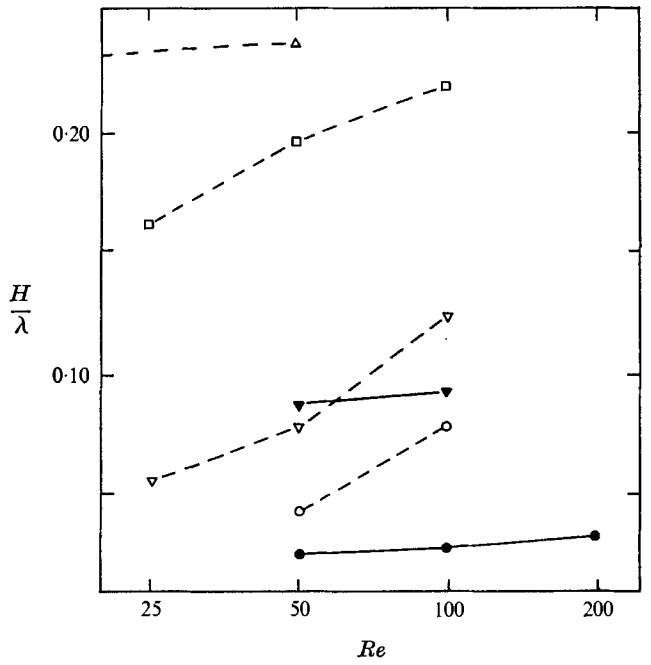

FIGURE 11. Effects of Reynolds and Richardson number on braid displacement. $\alpha = 0{\cdot}20$. J: ○, 0·03; △, 0·07. $\alpha = 0{\cdot}43$. J: ○, 0·03; △, 0·07; □, 0·15; ▽, 0·20.

shows a strong stabilizing effect. We note particularly how uninfluential viscosity is when the disturbance wavelength is very long (i.e. when α is small).

An additional, 'hidden' parameter of these simulations is the amplitude of the disturbance at $\tau = 0$. All runs represented in figures 4–11 were started with the same maximum initial slope ($-0{\cdot}20$) of the mean-density surface. Because of diffusion, the stability characteristics of the base flow change with time. The Richardson number increases, which is stabilizing; the Reynolds number increases, which is destabilizing; and α increases, which is either stabilizing or destabilizing depending on whether α is $\lesssim$ the value for most rapid disturbance growth. In two cases for which we made a test, disturbances that were initially weaker (maximum initial slope = 0·10) stayed weaker for all times. In these cases, the effect of growing α was stabilizing.

Although the climax states vary considerably in appearance, one of small amplitude tends to look rather like an intermediate state in a case destined to arrive at a larger amplitude. This suggests that some simplified kinematic model of the disturbed flow at any stage of development may be discovered, and that approximate correlations of fairly general utility exist between some important gross properties of the flow. One example is shown in figure 12, where the dimensionless shear across the braid midsection is plotted against the steepness ratio H/λ for all the climax states represented in figure 11. A systematic small dependence on α is seen, but variations of Reynolds and Richardson number seem only to displace points along the correlation curves. The solid curve represents

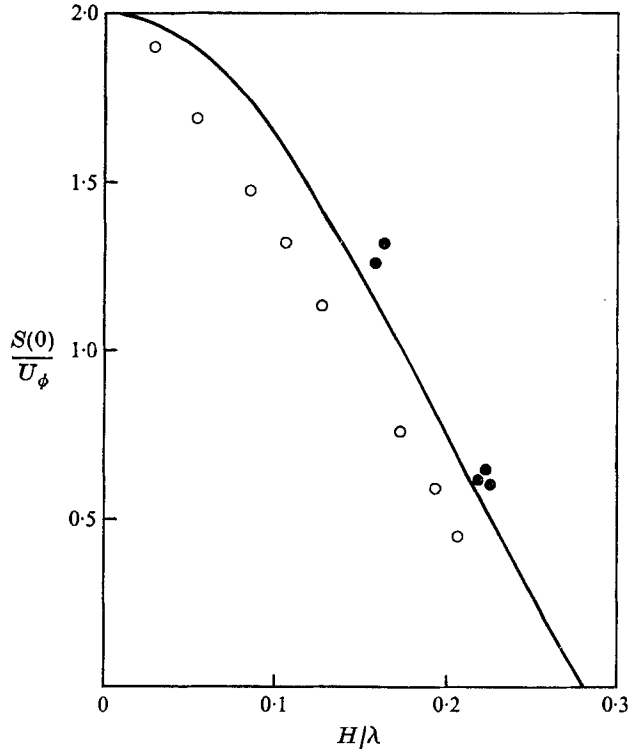

FIGURE 12. Kinematic correlation of climax states. α: ●, 0·20; ○, 0·43.

the kinematic model (Stuart 1967), of which use is made in Corcos & Sherman (1976).

5.4. *Late-time behaviour of a long wave*

It is clear, from a superposition of streamlines and isopycnic curves in the climax state, that this is not a state of permanent equilibrium, but that further dynamic developments must follow. These were traced out in one case, with results shown in figures 13–15. The superposed streamlines and equivorticity contours of figure 13 show the rapid development of a climax state, by about $\tau \equiv Ut/\lambda = 1{\cdot}3$, and the subsequent relaxation, by $\tau = 4{\cdot}0$, to a state which is nearly steady.

The events which follow the climax state are complex, and the following attempt to describe them admittedly infers a great deal from a single simulation.

We first try to unravel the roles of inertial, viscous and buoyancy forces, with the help of the equation

$$dE/dt = P + B - \epsilon.$$

Here E is the total disturbance energy defined in § 5.1; P and B are the rates of production of E due to Reynolds stresses and buoyancy forces respectively; and ϵ is the rate of viscous dissipation of E. The quadratures defining P and B are

$$\begin{Bmatrix} P(t) \\ B(t) \end{Bmatrix} = \int_{-0{\cdot}625\lambda}^{0{\cdot}625\lambda} \left(\begin{Bmatrix} \rho_0 \dfrac{\partial \overline{u}}{\partial y} \\ -g \end{Bmatrix} \int_0^{\lambda} \begin{Bmatrix} u - \overline{u} \\ \rho - \overline{\rho} \end{Bmatrix} v \, dx \right) dy.$$

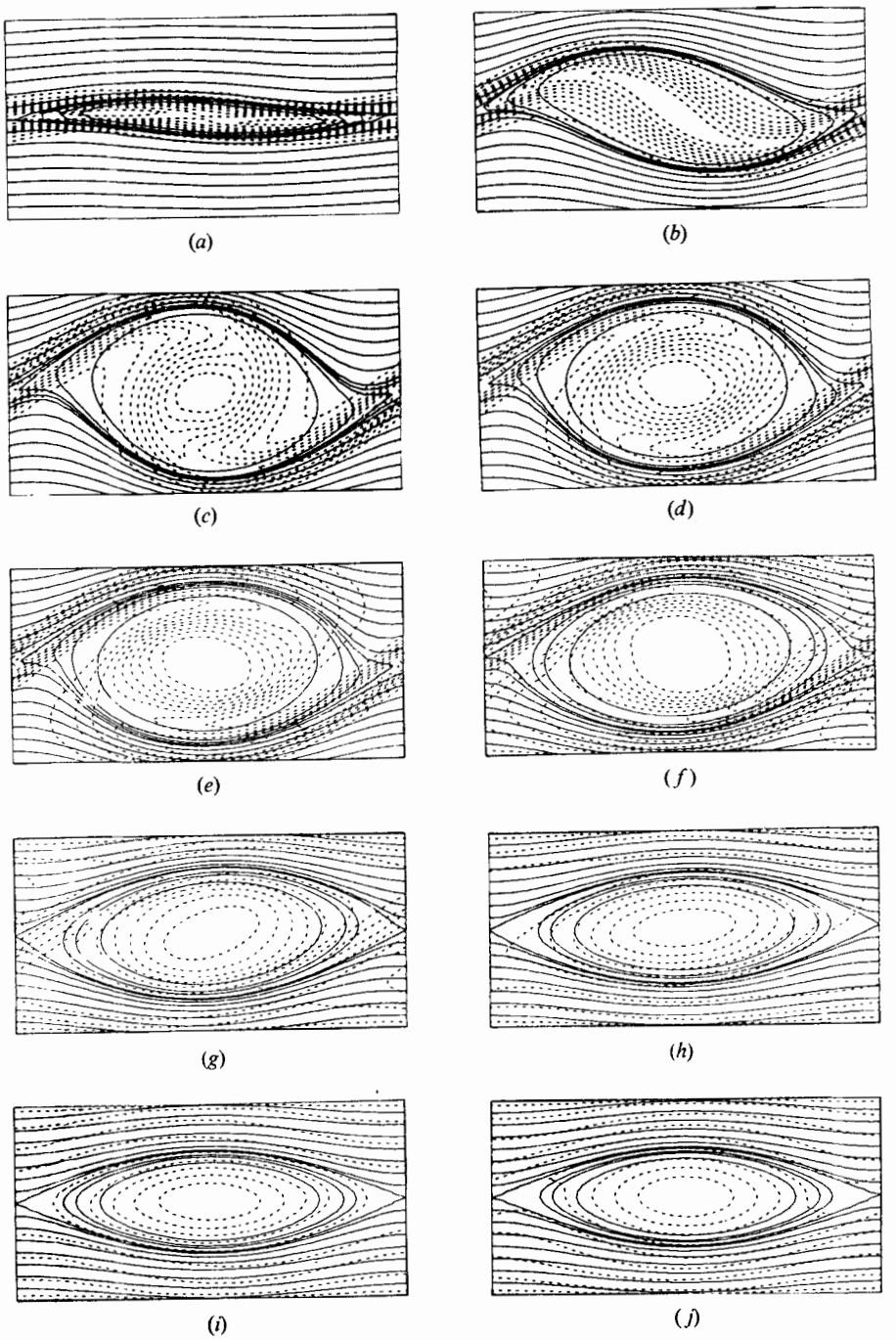

FIGURE 13. Flow evolution before and after the climax state. $\alpha = 0{\cdot}2$, $Re = 25$, $J = 0{\cdot}03$. ——, streamlines; – – –, equivorticity lines. τ: (*a*) 0, (*b*) 0·5, (*c*) 1·0, (*d*) 1·5, (*e*) 1·75, (*f*) 2·0, (*g*) 2·5, (*h*) 3·0, (*i*) 3·5, (*j*) 4·0.

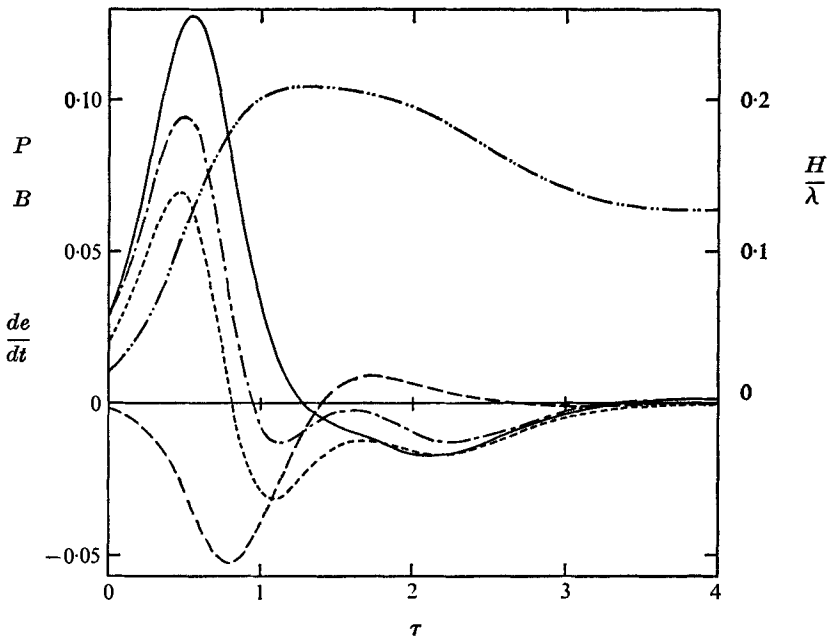

FIGURE 14. Energy balance before and after the climax state. $\alpha = 0{\cdot}2$, $Re = 25$, $J = 0{\cdot}03$. ——, energy transfer by Reynolds stresses, P; – –, energy transfer by buoyancy forces, B; –·–, $P+B$; – – –, rate of change of 'eddy kinetic energy', dE/dt; –· ·–, aspect ratio of cat's eye, H/λ.

In figure 14 we present P, B, $P+B$, dE/dt, and H/λ as functions of time. We see that P is positive and B is negative while H/λ is growing. During this time the kinetic energy extracted from the mean shear flow appears both as kinetic energy of the disturbance and as increased gravitational potential energy. A significant amount of disturbance energy is lost to viscous dissipation, but the qualitative trend of dE/dt is only slightly influenced by viscosity. During the latter part of the rise of the wave to its climax amplitude, disturbance kinetic energy is traded for potential energy to a significant degree.

In the relaxation process following the maximum of H/λ, some potential energy is fed back into E, and some of E is returned to the mean flow via the Reynolds stresses. By the time $\tau = 4$, P, B, and dE/dt have all settled down to very small values, and the rate of viscous dissipation has become particularly small as the sharp gradients become smoothed away.

It appears from this viewpoint that both the growth to the climax state, which features the rapid opening of the cat's eye and the entrainment of a considerable volume of fluid into this region of recirculating flow, and the subsequent relaxation, which exhibits a partial closing of the eye and the loss of some fluid from the recirculating region, are essentially inviscid processes. It seems rather likely that the relaxation involves a damped oscillation, the decay rate of which is set by viscosity. The oscillation could involve a periodic exchange between kinetic and potential energy, or simply a kinematic effect due to the rotation, within

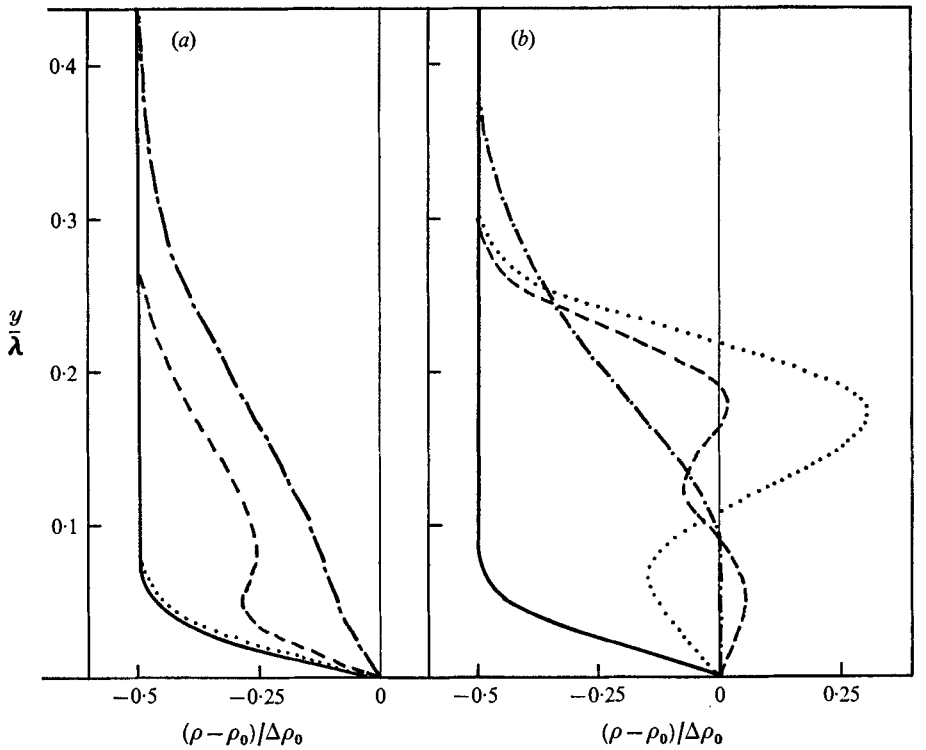

FIGURE 15. Flow evolution after the climax state. $\alpha = 0{\cdot}2$, $Re = 25$, $J_0 = 0{\cdot}03$, $Pr = 0{\cdot}72$. (*a*) Braid, $[\rho(0,y,t)-\rho_0]/\Delta\rho_0$. (*b*) Core, $[\rho(\frac{1}{2}\lambda,y,t)-\rho_0]/\Delta\rho_0$. τ: ——, 0; · · ·, 1·3; – – –, 2·0; –·–, 4·0.

the cat's eye, of a slightly elliptical distribution of vorticity. The latter phenomenon has appeared in the nominally inviscid-flow simulations of Zabusky & Deem (1971), who refer to it as a nutation.

Figure 15 shows the density distribution in vertical sections through a braid and a core, at various times. The initial profiles in the two sections are nearly the same. As the wave grows to a climax, the braid profile hardly changes, because in this particular case diffusive thickening has almost exactly cancelled advective thinning. Meanwhile, large intrusions of heavy fluid on top of light, which would be even more dramatic in a case with higher Re, have developed in the core. As the relaxation proceeds, diffusion smooths away the density contrasts in the core, until a nearly constant density is achieved there by time $\tau = 4$. The braids have also thickened greatly during this time, but a careful inspection of isopycnic maps shows that this is not the results of local diffusion, but of advective intrusions of fluid from neighbouring braids, which escaped entrainment into the intervening cores.

5.5. *Interaction between the fastest-growing wave and its first subharmonic*

The class of wave interactions that can conveniently be simulated with periodic boundary conditions in x is fairly limited, but we studied one interaction which

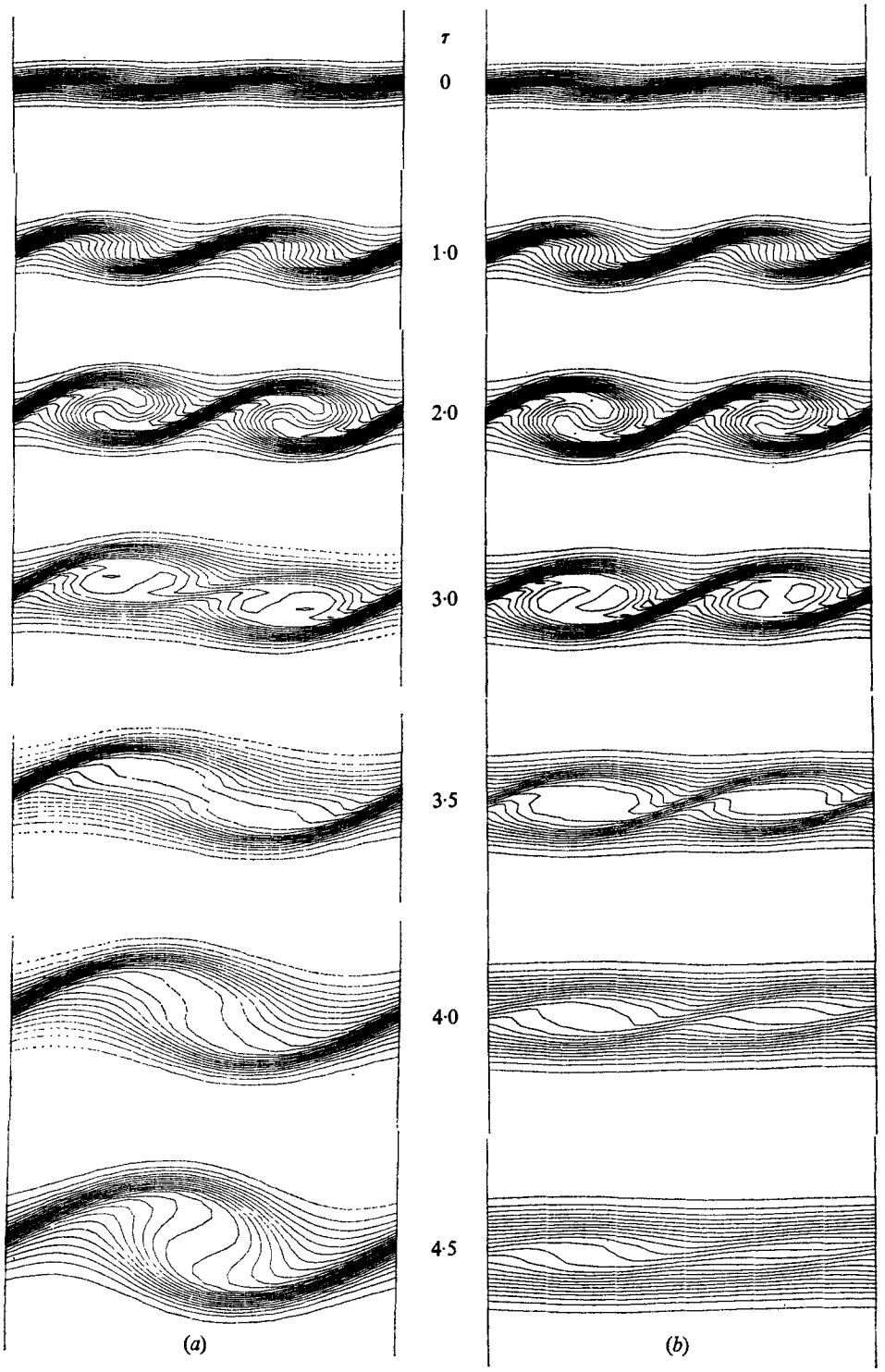

FIGURE 16. Resonant interactions with subharmonics (isopycnics). $\alpha = 0{\cdot}43$ and $0{\cdot}215$, $Re = 50$, $J_0 = 0{\cdot}07$, $Pr = 0{\cdot}72$. (*a*) Rolling interaction. (*b*) Shredding interaction.

appears frequently in laboratory studies,† and which seems to play a particularly important role in the growth of shear layers by entrainment. This is the interaction between the normal mode which grows fastest in the linear range and its first subharmonic. We could simulate this by doubling the horizontal length of our computational domain and adding an appropriate subharmonic disturbance into the initial conditions. This required a choice of the relative amplitudes and phase of the two disturbance components.

Figure 16 shows the evolving isopycnic patterns for two such simulations, in which $\alpha_S = 0{\cdot}43$, maximum initial slope of an isopycnic $= -0{\cdot}16$, $\alpha_L = 0{\cdot}215$, maximum initial slope of an isopycnic $= -0{\cdot}014$. The other parameters are $J = 0{\cdot}07$, $Re = 50$. The non-dimensional time τ is formed with the shorter wavelength. The ratio of initial amplitudes was selected to reflect the faster growth of the shorter wave in the linear range, on the assumption that both waves were equally excited at $\tau \simeq -30$, with 'infinitesimal' initial slopes of about -5×10^{-3}.

The interaction simulations involved four computer runs. First, each component wave was allowed to develop alone, from the initial amplitude given above. Then the two waves are superposed in the initial data, first with the core of the long wave midway between the cores of the short wave, resulting in the flow shown in figure 16(*a*), and again, with the core of the long wave centred on the left-hand core of the short wave (figure 16*b*).

The action of the long wave on the short is fundamentally different in the two combined-wave cases. In figure 16(*a*) the cores of the short wave are in locations where the long wave induces a simple pivoting translation around the centre of the picture, with very little straining motion. In figure 16(*b*) the right-hand core of the short wave is caught in the strain field midway between the incipient cores of the long waves and is eventually shredded away by that straining motion. In both cases, the short wave is eventually annihilated by its subharmonic.

5.6. *Secondary, smaller-scale instabilities*

In none of our simulations was there any indication of the onset of secondary, smaller-scale instabilities, either in the cores, where there are statically unstable regions, or in the braids, where a shear-driven instability of the Kelvin–Helmholtz type would be a possibility.

It is probably true that such instabilities are not to be expected at these rather low Reynolds numbers. For similar Reynolds numbers in a wind-tunnel experiment, Delisi & Corcos (1973) reported no signs of turbulence, although this does not quite rule out the possibility of small-scale instabilities, which might have reached a nearly identical state of development in each full-scale billow at the time it passed the measuring station.

It is almost certainly true that, even if such instabilities are physically possible within our range of overall parameters, they would not be revealed by our calculations because: (i) our initial data are unphysically free of small-scale perturbations; and (ii) our discrete space and time steps are too coarse to reveal instabilities on a scale much smaller (say perhaps 5 times smaller) than that of our

† See e.g. Browand & Wang (1972) or Winant & Browand (1974).

primary disturbances. For example, unphysical damping of numerically-simulated Tollmien–Schlichting waves, as a result of an excessively large time step, was documented by Fasel (1974).

6. Summary and conclusions

Out of all the detailed information the numerical simulations provide, we can extract some qualitative generalities, some of which are synthesized into an approximate theoretical model in Corcos & Sherman (1976). Others escape a simple theoretical description, but are of some intrinsic interest.

Concerning the growth of isolated normal modes, we observe the following.

(i) Growth at small amplitudes is in fair agreement with the predictions of a linear theory which assumes a parallel and time-independent base flow. Systematic deviations seem to lie in a direction which might be predicted by applying the linear theory to a quasi-steady base flow.

(ii) Growth is self-limiting because of the finite supply of vorticity available to a wave of fixed wavelength, and the necessary sharing of this vorticity, in baroclinic flows, between the cores and the braids.

(iii) Parametric variations (decreasing Re, increasing J, increasing α beyond 0·43) that inhibit wave growth in the linear range, also restrict the development of large maximum wave amplitudes. The unifying aspect of all these effects is that they inhibit (each in a distinctive way) the coalescence of vorticity into relatively compact cores. A related result is that relatively long waves, which coalesce vorticity very efficiently, grow much more impressively in the nonlinear range than would be expected by extrapolation of linear theory.

(iv) To a remarkable extent, states of small maximum amplitude resemble states through which the flow passes when a more favourable set of parameters allows further growth.

(v) The state of maximum amplitude (the climax state) is not one of equilibrium, but appears to represent the overshooting of a more stable state, to which the flow relaxes in a time comparable with that required to reach the climax. This relaxation may actually involve a damped oscillation, only the first cycle of which was visible because of low Reynolds number.

There has been relatively little analytical work devoted to the nonlinear stages of this problem, an exception being the work of Maslowe (1973). Following the ideas of Benney & Bergeron (1969), he found steady solutions of the Boussinesq equations which somewhat resemble the state towards which our waves relax after reaching maximum amplitude. Maslowe's theory involves asymptotic representations for high Reynolds number, presumably about an order of magnitude higher than those employed here, but perhaps within the range of accurate application of a specially-designed finite-difference simulation.

For barotropic flows, other types of asymptotic representations have been worked out for the free shear layer by Schade (1964) and Robinson (1974). The two lines of development are in some respects conceptually distinct, but they both embody the assumption that the dimensionless wavenumber α is close to one. This is in a sense an unfortunate point of departure for an asymptotic

expansion, since, if our results for $\alpha = 0{\cdot}6$ and $0{\cdot}7$ are at all indicative of the general behaviour of relatively short waves, such waves are individually of comparatively slight practical interest. (That is to say, they contribute very little to entrainment, and to subsequent mixing and thickening of the shear layer.)

Concerning the interaction of normal modes with one another, we make the following limited observations.

(vi) Within a limited range of stable stratification, that wave which grows most rapidly in the linear range will eventually be absorbed by its first subharmonic. This is likely to happen rather shortly after the shorter wave reaches its climax state, unless the initial state is unusually free of subharmonic content.

(vii) The kinematics of this subharmonic interaction depend dramatically on the phase relationship in which the two waves are initially superposed. In the more dramatic, 'pivoting', interaction, a significant amount of entrainment occurs. Seemingly this is somewhat more than would occur if the subharmonic wave grew alone.

A quantitative discussion of even this very limited class of interaction experiments is difficult, and we have decided to leave it for another paper, for which we are now accumulating computational data.

We are grateful to the National Science Foundation for partial support of this work under grant GA-35783 to the University of California, and for their support of the National Center of Atmospheric Research, where the additional computations represented in figures 13–16 were performed. We also thank Professor Alexandre Chorin for encouragement at crucial times.

Note added in proof. We should also like to draw readers' attention to recent work of Takata (1975), who used a *modal* rather than a finite-difference representation of x variations. His results would be of interest to those interested in the present paper.

REFERENCES

Amsden, A. A. & Harlow, F. H. 1964 *Phys. Fluids*, **7**, 327.

Batchelor, G. K. 1967 *An Introduction to Fluid Dynamics*. Cambridge University Press.

Benney, D. J. & Bergeron, R. F. 1969 *Stud. Appl. Math.* **48**, 181.

Browand, F. K. & Wang, Y. H. 1972 An experiment on the growth of small disturbances at the interface between two streams of different densities and velocities. *Proc. Int. Symp. on Stratified Flows*, Novosibirsk, USSR.

Browand, F. K. & Winant, C. D. 1973 *Boundary-Layer Met.* **5**, 67.

Chorin, A. J. 1968 *Math. Comp.* **22**, 745.

Chorin, A. J. 1969 *Math. Comp.* **23**, 341.

Christiansen, J. P. 1973 *J. Comp. Phys.* **13**, 363.

Corcos, G. M. & Sherman, F. S. 1976 *J. Fluid Mech.* **73**, 241.

Delisi, D. P. & Corcos, G. M. 1973 *Boundary-Layer Met.* **5**, 43.

Fasel, H. 1974 Untersuchungen zum Problem des Grenzschichtumschlages durch numerische Integration der Navier–Stokes Bleichungen. Dissertation, Institut A für Mechanik, University of Stuttgart.

GARRETT, C. & MUNK, W. 1972 *Deep-Sea Res.* **19**, 823.

MASLOWE, S. A. 1973 *Boundary-Layer Met.* **5**, 43.

MASLOWE, S. A. & THOMSON, J. M. 1971 *Phys. Fluids*, **14**, 453.

MAXWORTHY, T. & BROWAND, F. K. 1975 Experiments in rotating and stratified flows with oceanographic application. *Ann. Rev. Fluid Mech.* **7**, 273.

MICHALKE, A. 1965 *J. Fluid Mech.* **23**, 521.

PATNAIK, P. C. 1973 A numerical study of finite-amplitude Kelvin–Helmholtz waves. Ph.D. dissertation, Department of Mechanical Engineering, University of California, Berkeley.

ROBINSON, J. L. 1974 *J. Fluid Mech.* **63**, 723.

SCHADE, H. 1964 *Phys. Fluids*, **7**, 623.

STUART, J. T. 1967 *J. Fluid Mech.* **29**, 417.

TAKATA, H. 1975 *J. Met. Soc. Japan*, **53**, 1.

THORPE, S. A. 1971 *J. Fluid Mech.* **46**, 299.

THORPE, S. A. 1973 *Boundary-Layer Met.* **5**, 95.

WINANT, C. D. & BROWAND, F. K. 1974 *J. Fluid Mech.* **63**, 237.

WOODS, J. D. & WILEY, R. L. 1972 *Deep-Sea Res.* **19**, 87.

ZABUSKY, N. J. & DEEM, G. S. 1971 *J. Fluid Mech.* **47**, 353.